

Deep-learning-based Q model building for high-resolution imaging

Xin Ju¹  | Jincheng Xu^{1,2} | Jianfeng Zhang^{1,2}

¹Department of Earth and Space Sciences, Southern University of Science and Technology, Shenzhen, China

²Guangdong Provincial Key Laboratory of Geophysical High-resolution Imaging Technology, Shenzhen, China

Correspondence

Jincheng Xu and Jianfeng Zhang,
 Department of Earth and Space Sciences,
 Southern University of Science and
 Technology, Shenzhen, 518055, China.
 Email: xujc@sustech.edu.cn and
zhangjf@sustech.edu.cn

Funding information

National Key R&D Program of China,
 Grant/Award Number: 2020YFA0713402;
 National Natural Science Fund of China,
 Grant/Award Numbers: 42174128,
 42030802; Guangdong Provincial Key
 Laboratory of Geophysical High-resolution
 Imaging Technology, Grant/Award Number:
 2022B1212010002

Abstract

Building a macro Q model for deabsorption migration using surface reflection data is challenging owing to interferences of the reflections resulting from stacked thin layers. The effective Q approach gives an alternative way to overcome this difficulty. However, manual processing is involved for effective Q estimation. This restricts the use of denser grids in building an inhomogeneous Q model. We therefore incorporate deep learning into the effective Q approach, thus yielding a deep learning-based Q model building scheme. The resulting scheme improves the manual effective Q estimation by simultaneously accounting for the imaging resolution and induced noises using two networks. Moreover, most manual processing is reduced in spite of denser grids in building a 3D Q model. One of the networks used is a 1D convolutional neural network that determines the optimal upper cut-off frequency for a selected Q with an input of multi-channel amplitude spectra, and another is a residual neural network that determines the optimal Q for a series of Q values with an input of multi-channel imaging sections inside the selected small window filtered under the corresponding upper cut-off frequencies. As a result, a Q model that improves the imaging resolution in the absence of amplification of noises is gained. Transfer learning is used, thus reducing the training cost when applied to different geological targets. We test our scheme using 3D field data. Higher resolution images without induced noises are obtained by a deabsorption migration using the Q model built and compared to those obtained by the migration without absorption compensation.

KEYWORDS

Attenuation, Modelling, Imaging

INTRODUCTION

The anelasticity of subsurface media results in the attenuation and dispersion of seismic waves, leading to the loss of high-frequency energy and affecting the seismic imaging resolution. The quality factor Q is used to quantitatively describe the attenuation characteristics (Aki & Richards, 1980). Many Q -compensated methods have been developed to restore attenuated amplitude and correct dispersion based on an appropriate Q model (Li, J et al., 2024; Mittet et al., 1995;

Qu et al., 2021, 2022; Sun et al., 2016; Zhang & Wapenaar, 2002; Zhu et al., 2014). Traditional Q estimation methods mainly use the Vertical seismic profiling (VSP) and crosswell data, such as the spectral ratio method and peak frequency shift method (O'Brien & Lucas, 1971; Gladwin & Stacey, 1974). However, they are not always available and sufficient to build a 3D inhomogeneous Q model. One feasible approach is using surface reflection data. However, stacked thin layers will strongly interfere with the waveform of seismic data, causing notches and peak frequency shifts (Zhang et al., 2013). It is

hard to determine whether the changes in wavelets are caused by interference effects or intrinsic attenuation. Although some papers have been published on Q estimation from surface reflection data (Dasgupta & Clark, 1998; Xin & Hung, 2009), the problem of interference effects remains unresolved. To address this issue, Zhang et al. (2013) proposed an approach for building a macro inhomogeneous Q model in deabsorption prestack time migration (QPSTM), instead of building an interval Q model, building an effective Q model from surface reflection data with scanning techniques. Unlike the proposed Q estimation methods, which only consider a single criterion such as spectrum or wavelet, this approach comprehensively considers compensation effect and amplitude spectrum. In the proposed approach, the frequency-dependent traveltime and amplitude of the imaging point are only dependent on the effective Q parameter (Q_{eff}) and root mean square velocity at that point. Therefore, by selecting a spatial-temporal window on the compensated section and evaluating the imaging resolution and noise level, the Q_{eff} at the centre of the window can be determined (Wang et al., 2017). Additionally, using the stacked spectra (time window) instead of the single spectrum (single seismic trace) effectively suppresses the interference effects.

We expect that Q compensation can enhance imaging resolution and compensate for high-frequency components. However, real seismic data always have a low signal-to-noise and prominent high-frequency noise. Q compensation tends to inevitably enhance high-frequency noise. Therefore, it is necessary to determine an upper cut-off frequency ($F3$) simultaneously based on the noise level of the compensated section. Different Q compensation requires different $F3$ for suppression. This implies that the Q_{eff} and $F3$ are coupled, leading to difficulty in determining a suitable combination from numerous combinations. Furthermore, the comprehensive consideration of the compensation section and spectra imposes limitations on the utilization of denser grids in building an inhomogeneous Q model.

Compared to conventional prestack time migration (PSTM), QPSTM is very time-consuming, which hinders its practical application in large-scale 3D seismic exploration. To alleviate the computational burden, Zhang et al. (2016) introduced a stationary-phase implementation approach in the angle domain optimization of imaging aperture in the 3D QPSTM scheme. Xu et al. (2018) proposed a parallel computing scheme for 3D stationary-phase QPSTM based on GPU/CPU heterogeneous parallel computing, significantly improving the computational efficiency of 3D QPSTM. Another crucial step in QPSTM is to build a Q model. In practical applications, the time cost of building a 3D Q model corresponding to a 3D imaging volume is substantial.

In recent years, deep learning has achieved remarkable success in diverse domains, including computer vision and natural language processing. Deep learning employs intricate

network structures comprising interconnected nonlinear ‘neurons’ to model the complex nonlinear mapping relationship between input feature sets and the corresponding expected outputs (LeCun et al., 2015) and can further make effective predictions for new inputs. Among various neural network structures, convolutional neural networks stand out as the most popular, and they have been extensively utilized in seismology. These deep learning-based methods encompass tasks such as first arrival picking (Wang et al., 2019), velocity analysis (Park & Sacchi, 2020) and high-resolution seismic imaging (Liu et al., 2020; Zhou et al., 2022). They successfully express the nonlinear mapping relationship between input feature sets (seismic waveforms, velocity spectra and conventional PSTM seismic result) and the expected outputs (first arrival, velocity model and deabsorption PSTM seismic result). There has been some research on Q estimation using deep learning. Yildirim et al. (2017) compared the performance of different Q estimation methods, including the artificial neural network, amplitude decay, spectral ratio and Wiener filter, tested on noise-free and noisy synthetic data. The results indicate that the artificial neural network method exhibits higher accuracy. Zhang et al. (2021) used the U-Net to predict the strong attenuation probability from marine reflection seismic data, thereby deriving an anomalous Q model. Wang et al. (2021) proposed a multitask learning-based dynamic wavelet amplitude spectra extraction method and applied it for interval- Q estimation. Zhang et al. (2022) used the fusion neural network to estimate the interval- Q value. Wu et al. (2024) used a back-propagation neural network to estimate the Q value from post-stack imaging data without Q compensation. Li, F et al. (2024) proposed a fully connected network-based method to extract interval- Q using VSP seismic data. However, deabsorption migration requires a macro Q model using an effective Q approach (Zhang et al., 2013), rather than a strong attenuation probability (Zhang et al., 2021) or interval- Q value (Wang et al., 2021; Zhang et al., 2022; Li, F et al., 2024). In addition, none of the above methods consider the high-frequency noise enhanced by compensation. We incorporate deep learning into the effective Q approach, improving the manual effective Q estimation by accounting for the imaging resolution and induced noises simultaneously. The manual effective Q estimation involves identifying the nonlinear mapping relationship from seismic sections and spectra (input feature) to the corresponding Q value and $F3$ (expected outputs). Harnessing the power of deep learning, we can perform Q estimation with enhanced efficiency. During training, the network autonomously learns the intricate nonlinear mapping relationship from a substantial amount of seismic section and spectra data, enabling it to effectively predict new inputs.

In this study, we proposed a deep learning-based scheme for building a macro Q model to address the difficulties associated with manual picking, such as the concurrent deter-

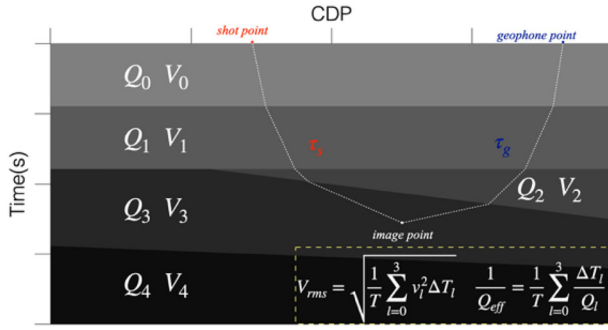


FIGURE 1 Illustration of effective Q value. τ_s , τ_g represent the travel time from the source point and geophone point to the image point. Q_{eff} represents the average absorption effect from the shot point or geophone point to the image point. CDP, common depth point.

mination of Q_{eff} and $F3$ and the substantial workload it entails. First, we review the principles of building a Q model from surface reflection data using scanning techniques. Second, we discuss the network structure, the loss function, the dataset and the training process. Finally, we applied the proposed scheme to a real field dataset from another region using transfer learning.

DEABSORPTION PRESTACK TIME MIGRATION AND EFFECTIVE Q

The formula for Q model in deabsorption prestack time migration can be expressed as follows:

$$I(x, y, T) = \left(\frac{\tau_s}{\tau_g} \right)^2 \int F(\omega) \exp \left(-j \frac{\pi}{2} \right) \quad (1)$$

$$\times \exp \left[j \omega (\tau_s + \tau_g) \left(1 - \frac{\ln \left(\frac{\omega}{\omega_0} \right)}{\pi Q_{\text{eff}}} \right) \right] \quad (1)$$

$$\times \exp \left[\frac{\omega}{2 Q_{\text{eff}}} (\tau_s + \tau_g) \right], \quad (1)$$

where (x, y, T) represents the positional coordinates of the image point, and τ_s, τ_g represent the travel time from the source point and receiver point to the imaging point. Q_{eff} is similar to the root mean square velocity, V_{rms} and represents the average absorption effect from the surface to the image point. They can be expressed as follows (as shown in Figure 1):

$$\frac{1}{Q_{\text{eff}}} = \frac{1}{T} \sum_{l=1}^n \frac{\Delta T_l}{Q_l}, \quad V_{\text{rms}} = \sqrt{\frac{1}{T} \sum_{l=1}^n v_l^2 \Delta T_l}, \quad (2)$$

where Q_l and V_l represent the interval Q and velocity of the overlying layers, respectively, whereas ΔT_l represents the vertical traveltime thickness of each layer, and $\exp[\frac{\omega}{2 Q_{\text{eff}}} (\tau_s + \tau_g)]$ is the compensation factor for the amplitude absorption and attenuation of seismic waves. Equation (1) indicates that the compensation factor at an image point is uniquely determined by Q_{eff} . Therefore, scanning techniques can be used to determine the Q_{eff} .

Q compensation not only enhances components within the effective frequency range but also compensates for high-frequency noise. However, interference effects hinder the accurate measurement of frequency bandwidth. To mitigate the interference effects during the determination of Q_{eff} , a spatial-temporal window is employed instead of a single seismic trace. Rather than utilizing a single spectrum, the stacked spectrum of the window is employed, manifesting fewer notches compared to a singular spectrum and thereby facilitating the measurement of frequency bandwidth. Figure 2 shows a typical time window for picking Q_{eff} and $F3$. Figure 2a is a Q compensated window, which contains many thin layers. Figure 2b is the stack spectrum of the window in Figure 2a. It is observed that high-frequency noise induced by Q compensation necessitates the determination of the $F3$ for suppression.

Q ESTIMATION BASED ON DEEP LEARNING

Network architecture

Traditional manual scanning techniques require a large number of classifications, making it difficult to pick a suitable Q_{eff} and $F3$ combination from a vast array of options. Deep learning has shown remarkable performance in image classification problems in recent years, particularly in complex multi-classification problems, surpassing human recognition capabilities. Convolutional neural network (CNN) is widely employed in computer vision and image recognition tasks due to their deep learning capabilities. CNN is designed to mimic the human visual system by employing stacked convolutional layers and pooling layers to effectively learn and extract features from images. This hierarchical structure allows for the gradual learning of more complex features at higher levels, starting with the acquisition of low-level features such as edges and textures in the initial layers and progressing to higher level features. The learning process gradually reveals the inherent features of the image. Additionally, CNN can process 1D data. CNN is capable of learning local patterns and structures in 1D spectra data. The lower level convolutional layers focus on relatively localized frequency patterns, whereas the higher level convolutional layers

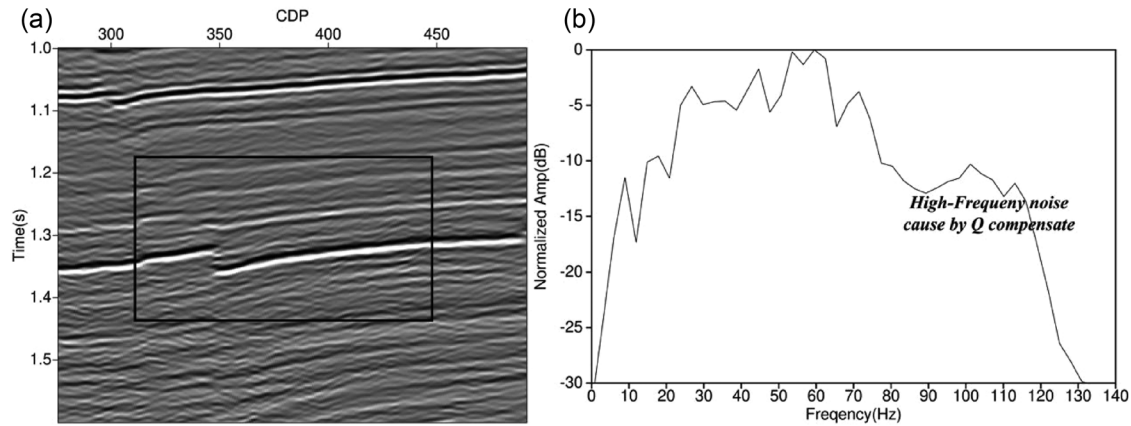


FIGURE 2 Illustration of a typical time window for picking Q_{eff} and $F3$. Panel (a) is a typical compensated window that contains many thin layers. Panel (b) is the stack spectrum of the rectangle in Panel (a). Observed that high-frequency noise cause by Q compensation; hence, the $F3$ is requisite to suppress that. CDP, common depth point.

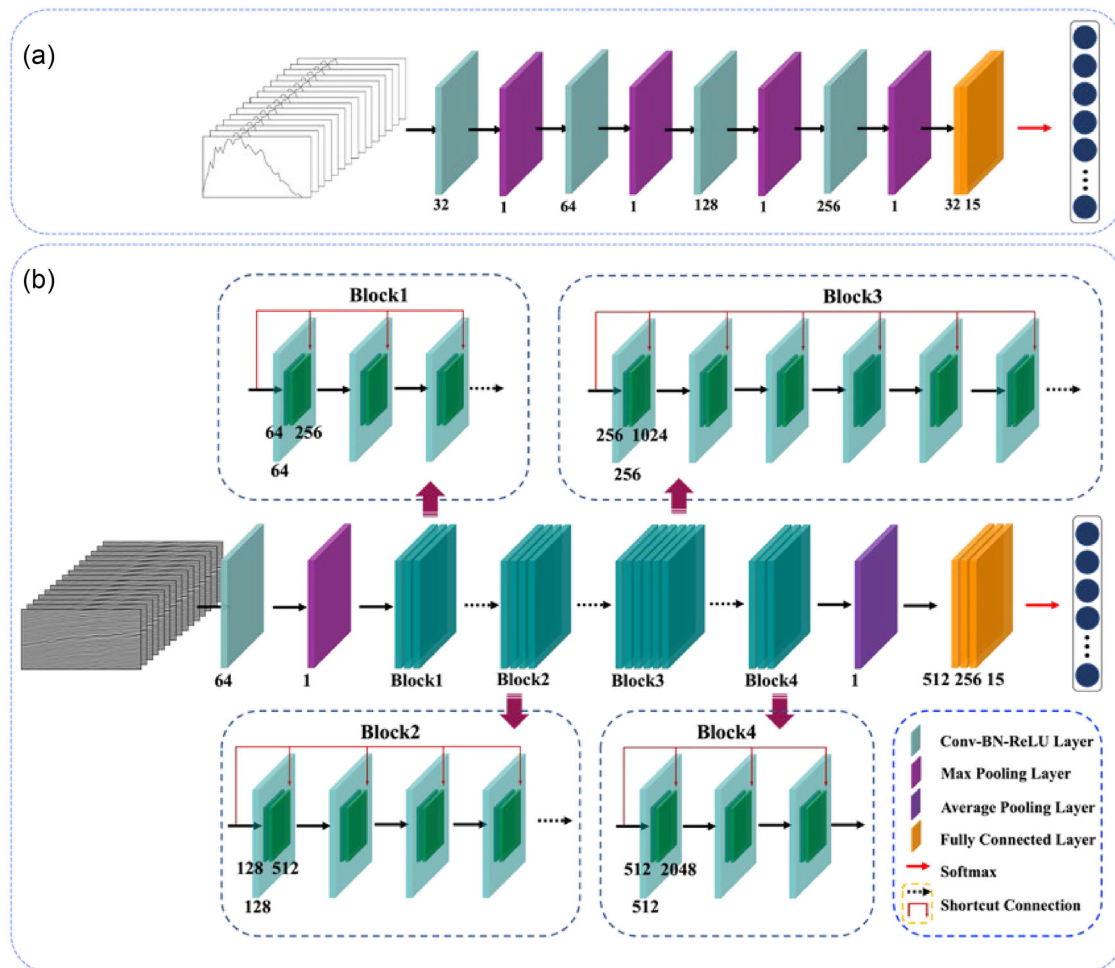


FIGURE 3 Panel (a) is the Network-A architecture, which consists of three alternating convolutional layers, pooling, and two fully connected layers. Panel (b) is the Network-B architecture, which consists of 4 residual blocks, 49 convolutional layers, 1 average pooling layer and 3 fully connected layers.

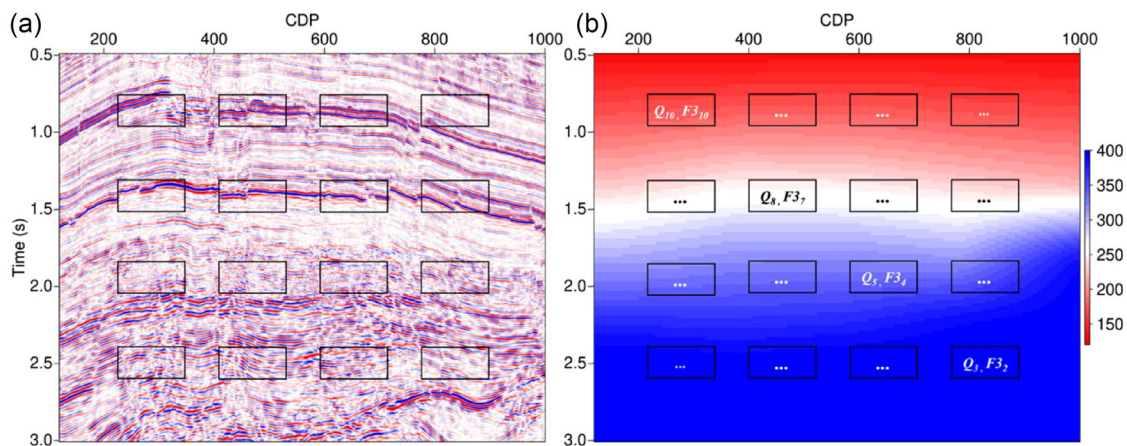


FIGURE 4 Training data and label generation process. Panel (a) is the Q model in deabsorption prestack time migration (QPSTM) migration stacked section of Line 300. Panel (b) is the Q_{eff} model with manual picking, which is used for migration in Panel (a). For one window in Panel (a), the time window and its spectrum are the inputs for Network-B and Network-A. Corresponding Q_{eff} and $F3$ in Panel (b) is the label for Network-B and Network-A. CDP, common depth point.

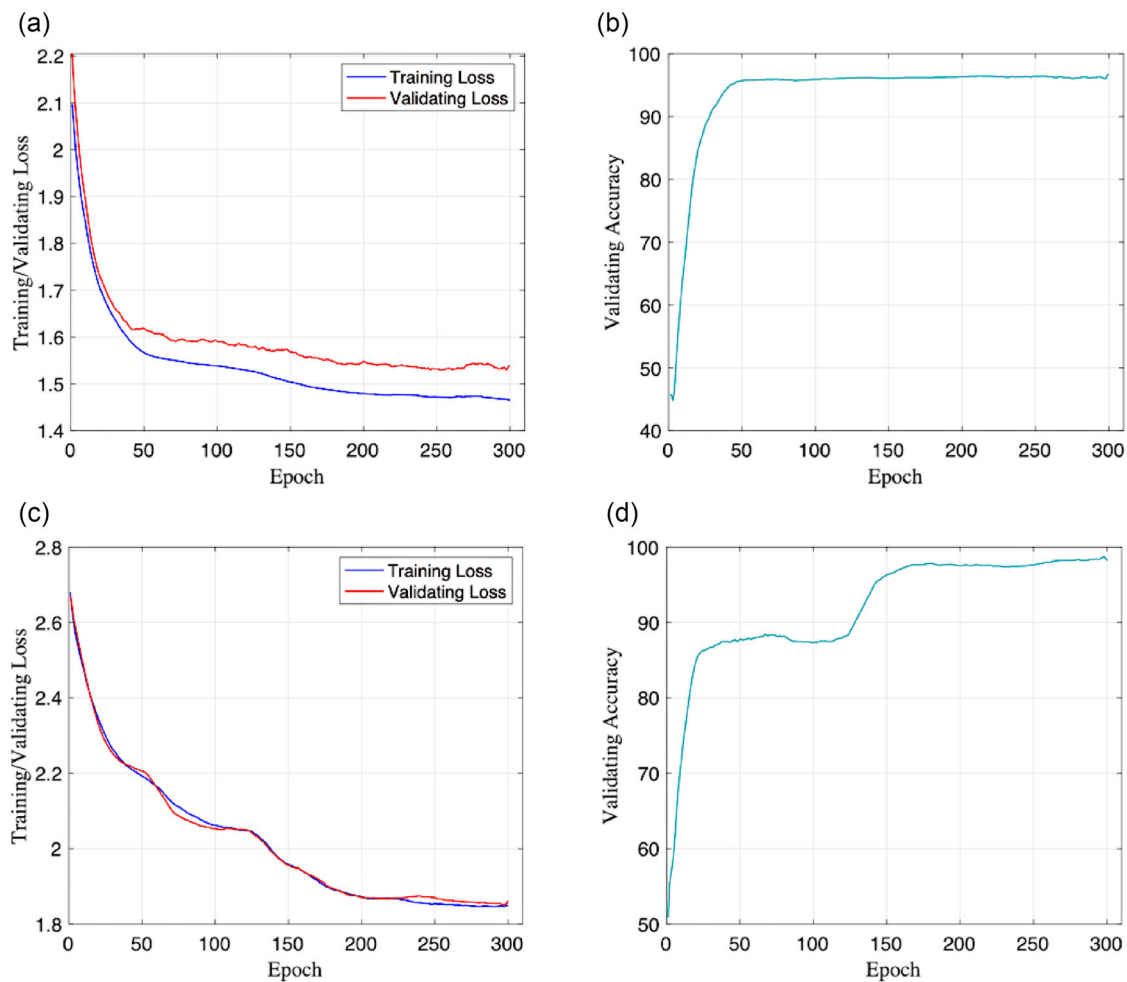
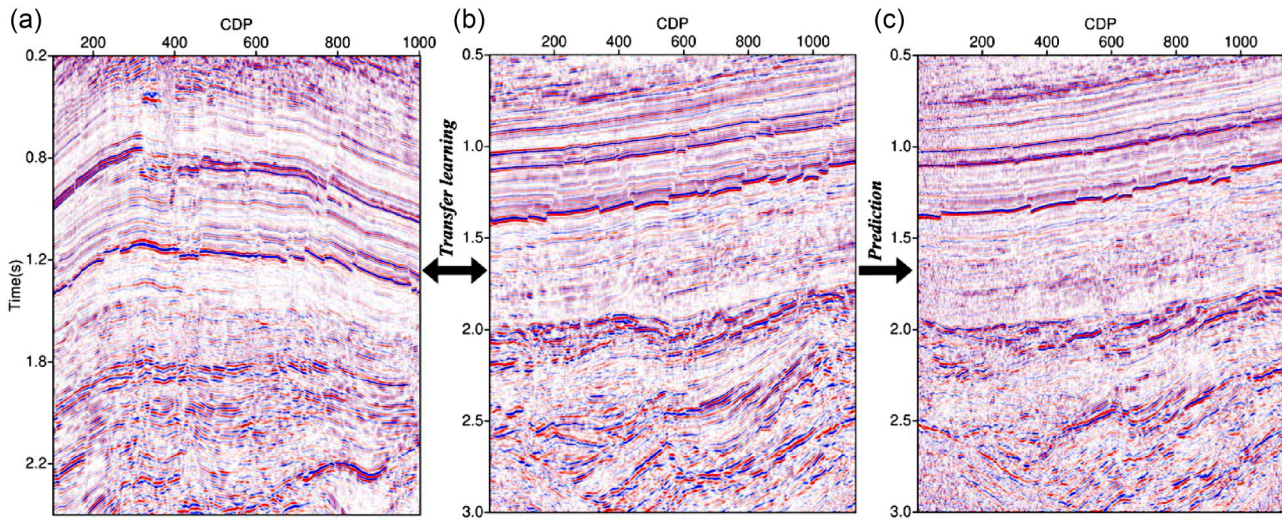


FIGURE 5 The training loss, validation loss, and validation accuracy. Panels (a) and (b) present the training loss, validation loss, and validation accuracy of Network-A. Panels (c) and (d) present the corresponding metrics for Network-B. The results showcase gradual convergence of prediction and a decrease in loss as the training iterations increase.

TABLE 1 Parameters of each layer for Network-A and Network-B.

Network-A			Network-B		
Layers	Structure	Output size	Layers	Structure	Output size
Input	–	(15,256)	Input	–	(15,128,256)
Conv2D-1	$3 \times 3, 32$	(32,128)	Conv2D	$3 \times 3, 64$	(64,128,256)
Maxpool2D-1	3×3	(32,64)	Maxpool2D	3×3	(64,64,128)
Conv2D-2	$3 \times 3, 64$	(64,32)	Block-1	$\begin{bmatrix} 1 \times 1, 64 \\ 3 \times 3, 64 \\ 1 \times 1, 256 \end{bmatrix} \times 3$	(256,64,128)
Maxpool2D-2	3×3	(64,16)	Block-2	$\begin{bmatrix} 1 \times 1, 128 \\ 3 \times 3, 128 \\ 1 \times 1, 512 \end{bmatrix} \times 4$	(512,32,64)
Conv2D-3	$3 \times 3, 128$	(128,8)	Block-3	$\begin{bmatrix} 1 \times 1, 256 \\ 3 \times 3, 256 \\ 1 \times 1, 1024 \end{bmatrix} \times 6$	(1024,16,32)
Maxpool2D-3	3×3	(128,4)	Block-4	$\begin{bmatrix} 1 \times 1, 512 \\ 3 \times 3, 512 \\ 1 \times 1, 2048 \end{bmatrix} \times 3$	(2048,8,16)
Conv2D-4	$3 \times 3, 256$	(256,2)	Avgpool2D	–	(2048,1,1)
Maxpool2D-4	3×3	(256,1)	Linear-1	512	(512,1,1)
Linear-1	32	(32)	Linear-2	256	(256,1,1)
Linear-2	15	(15)	Linear-3	15	(15)
Softmax	–	(15)	Softmax	–	(15)

**FIGURE 6** Illustration of transfer learning. Panel (a) shows the training data on Line 300. Panel (b) shows the transfer of learning data from another region on Line 415. Panel (c) shows the prediction data from the same region as Panel (b) on Line 350. Note that the regional subsurface structure of the training data is very different from that of transfer learning and prediction. Transfer learning was performed on the existing network using data from Line 415. Using the predicted Q_{eff} model as shown in Figure 8, the high-resolution imaging results are obtained. CDP, common depth point.

capture more abstract frequency structures. This enables more accurate classification. The parameter-sharing property of CNN enables the capturing of similar features across different inputs, resulting in reduced parameter count and improved model generalization ability. Estimating Q_{eff} using deep learning involves identifying the nonlinear mapping relation-

ship from seismic sections and spectra (input feature) to the corresponding Q_{eff} and $F3$ (expected outputs) as follows:

$$F3 = f_A(\text{spectra})$$

$$Q_{\text{eff}} = f_B(\text{sections})$$

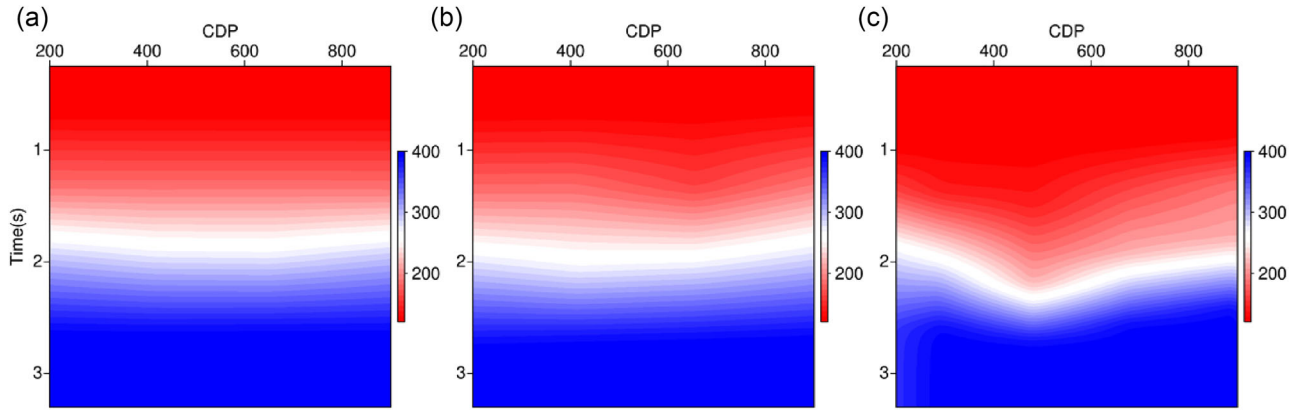


FIGURE 7 Comparison of Line 350 effective Q model obtained by manually picked (a), predicted by back-propagation neural network (BPNN) (b) and predicted by our approach (c). The Q fields are relatively consistent in most regions. Note the Q value in Panel (c) between 1.5 and 2.5 s shows more variations indicating the subsurface detail information compared to Panels (a) and (b). CDP, common depth point.

$$Q_{\text{eff}}^*, F3^* = \text{Combine}(Q_{\text{eff}}, F3). \quad (3)$$

In this study, the estimation of Q_{eff} is approached as two multi-classification problems using Network-A and Network-B. Within a given window, Network-A is used to determine the optimal $F3$ for a given Q_{eff} . Because $F3$ primarily impacts the frequency bandwidth, Network-A uses the spectrum of the section with identical Q_{eff} but varying $F3$. As illustrated in Figure 3a, Network-A utilizes 1D convolutional layers to extract features from input. Max pooling layers are employed to downsample and reduce the parameter count. Following three alternating layers of convolution and pooling, deep-level features are extracted and condensed into a fixed-length vector, reducing the length of the features to one. Following that, two fully connected layers are used, and the final output, which represents a multi-probability distribution indicating the likelihood of each sample belonging to each category, is generated with the Softmax activation function.

Network-B is used to determine the optimal Q_{eff} , which primarily impacts imaging resolution. Therefore, it suffices to choose the default $F3$ ($F3_{\text{max}}$). The input to Network-B consists of multi-channel sections composed of varying Q_{eff} with $F3_{\text{max}}$. Seismic sections encompass valuable feature information, including amplitude, frequency and phase. Extracting effective features from seismic sections using deep learning is challenging. Increasing the depth of neural networks directly enhances the learning capacity. However, beyond a certain depth, there is a potential for a sudden decline in accuracy, referred to as ‘Degradation’ (He et al., 2016). Residual blocks in residual neural network (ResNet) effectively address the degradation problem.

The fundamental concept is to directly integrate the data from specific layers into the input of subsequent layers, allowing later feature layers to partially depend on the contribution of earlier layers (He et al., 2016). The complexity of seismic

sections necessitates the utilization of deep neural networks. As a result, Network-B is constructed based on ResNet-50, wherein residual connections within each residual block combine the initial input with the features acquired through convolutional operations, thus effectively propagating gradient information. Learning from multiple residual blocks enables the model to extract more complex and abstract features. Following that, adaptive average pooling is used to reduce the spatial dimensions of the features to 1×1 . The features are then processed through three linear fully connected layers, yielding a low-dimensional output. Finally, the output layer uses the Softmax activation function to generate a probability distribution with multiple categories indicating the likelihood of each sample belonging to a specific category, as shown in Figure 3b.

Table 1 shows the details for each layer in Network-A and Network-B. Furthermore, the residual block structure is shared throughout the entire network. This means that the same residual block structure is used at each position in the network. This sharing property allows learned parameters and features across various positions in the network. Using this sharing property, ResNet can acquire universal feature representations that are more adaptable to diverse seismic section data. As a result, ResNet can generalize more effectively to novel seismic data, improving the adaptability and generalization capabilities of the network.

The cross-entropy function is chosen as the loss function to address this multi-classification problem (DeBoer et al., 2005). Cross-entropy, initially employed in information theory for estimating average encoding length, is used in deep learning to quantify the challenge of representing the probability distribution $p(x)$ using an alternative distribution $q(x)$. It measures the divergence between two probability distributions, with lower cross-entropy indicating a greater similarity between the distributions. The cross-

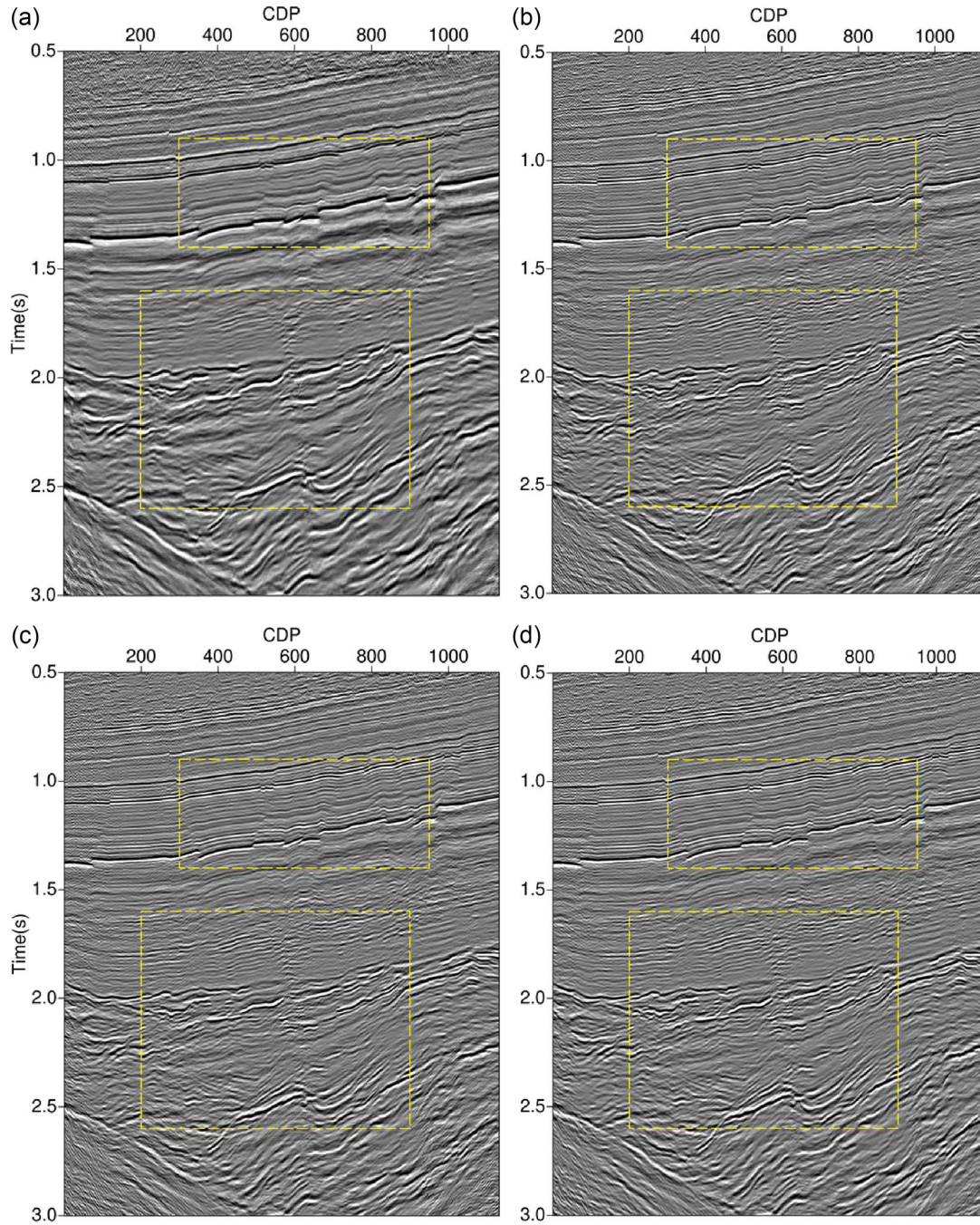


FIGURE 8 Comparison of Line 350 migration stacked sections obtained by conventional prestack time migration (PSTM) (a), Q model in deabsorption prestack time migration (QPSTM) with manually picked Q model (b), QPSTM with predicted Q model by back-propagation neural network (BPNN) (c) and QPSTM with predicted Q model by our approach (d). The QPSTM results using an effective Q model are shown in Figure 7, respectively. Note the resolution of the QPSTM result is enhanced compared to Panel (a). The upper and lower boxes indicate the enlarged detail in Figures 9 and 10. CDP, common depth point.

entropy function, designed for multi-classification problems, is an extension of the binary classification problem. The loss function is expressed as follows:

$$\text{Loss} = - \sum_{i=0}^{C-1} y_i \log(p_i) = -\log(p_c). \quad (4)$$

The probability distribution $p = [p_0, \dots, p_{C-1}]$ contains the probability of the sample belonging to each class i . The one-hot representation $y = [y_0, \dots, y_{C-1}]$ is used to indicate the sample label, with $y_i = 1$ if the sample belongs to class i and $y_i = 0$ otherwise. C represents the total number of classes. The cross-entropy loss function is employed to compute the error between the predicted probabilities and the label prob-

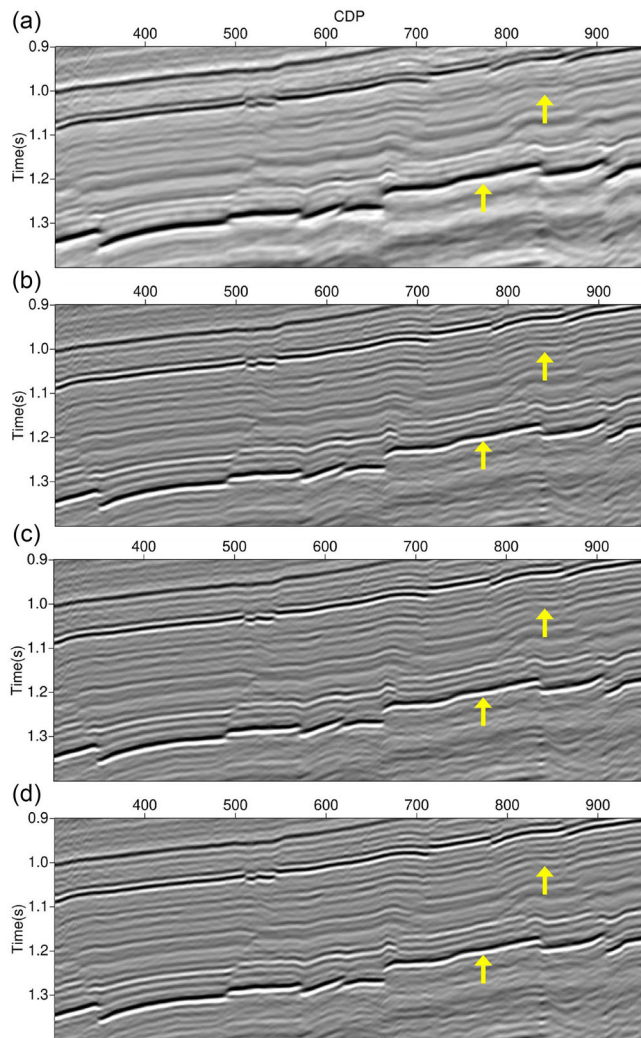


FIGURE 9 Comparison of the enlarged details in the upper box of Figure 8. Panel (a) shows the shallow migration result obtained by conventional prestack time migration (PSTM). Panels (b)–(d) show the shallow migration results obtained by Q model in deabsorption prestack time migration (QPSTM) in Figure 8b–d. Note the three QPSTM results have higher resolution and the events are separated, as indicated by the arrow. The comparison of the amplitude spectrum is shown in Figure 11a. CDP, common depth point.

abilities. Data normalization was carried out before training to enhance training convergence speed and reduce data discrepancies. The Adam optimizer was chosen as the parameter optimization algorithm.

Dataset and training

As our scheme is data-driven, we use real 3D field data to train and validate. The data size is 3 (lines) \times 1200 (CDPs) \times 6000 (samples), with a common depth point (CDP) interval of 20 m and a time sampling interval of 1 ms. The Q_{eff} sequence is obtained as the reciprocal of 15 Q values ranging from 0.0025 to 0.01 with equal intervals (Q_{eff} varies from 400

to 100). The upper cut-off frequency $F3$ values range from 50 to 120 Hz with 5 Hz interval, resulting in a total of 15 values. We use constant Q scanning with varying $F3$ performed on three lines: Line 200, Line 450 and Line 500, yielding 15 sets of constant $F3$ gathers with varying Q_{eff} values. Figure 4 shows the training data and label generation process. Figure 4a is the migration stacked section of Line 450 using the effective Q model (as shown in Figure 4b) with manual picking. For one window in Figure 4a, the time windows and their spectra are the input for Network-B and Network-A. Corresponding Q_{eff} and $F3$ in Figure 4b are the labels for Network-B and Network-A. Following the selection of identical time windows in seismic sections, where the window size is 128×256 , where 128 represents the number of CDPs, whereas 256 represents the number of imaging points in the time-depth dimension. The corresponding averaged amplitude spectra for the window are 256×1 , where 256 denotes the number of samples in the spectrum. The multi-channel spectra data are used in Network-A. The multi-channel section data are used for Network-B. In the end, we obtained 1050 samples for Network-A and 560 samples for Network-B. The dataset is divided into a training set and a validation set with an 8:2 ratio.

We conducted experiments and evaluations to improve the performance of the deep learning model and improve training efficiency and convergence speed. We focused on two critical parameters: batch size and learning rate (He et al., 2019). The impact of batch size was investigated by comparing smaller and larger batch sizes. Smaller batch sizes resulted in unstable parameter updates, significant training fluctuations and convergence challenges to the optimal solution. Larger batch sizes, on the other hand, demonstrated better hardware parallelism utilization and faster training, but they also increased the risk of local optima trapping, which resulted in lower performance or weaker generalization. After considering hardware resource utilization, stability and generalization capability, a batch size of 16 was determined to be the optimal choice. The effect of learning rate was investigated through experiments with both larger and smaller values.

Larger learning rates resulted in excessive parameter updates, causing the model to skip the optimal solution during training, resulting in convergence failure or erratic oscillations. In contrast, smaller learning rates resulted in slower training progress but required more iterations to achieve satisfactory performance. To enhance the training performance of Network-A and Network-B, a learning rate of $5E-4$ was chosen for Network-A due to its capacity to achieve faster convergence and higher performance. For Network-B, a smaller learning rate of $5E-7$ was chosen, considering that large-scale deep networks like ResNet-50 generally benefit from lower learning rates for optimization.

The parameter selection was finalized through extensive experimentation and comprehensive evaluation of diverse batch sizes and learning rates, resulting in faster convergence

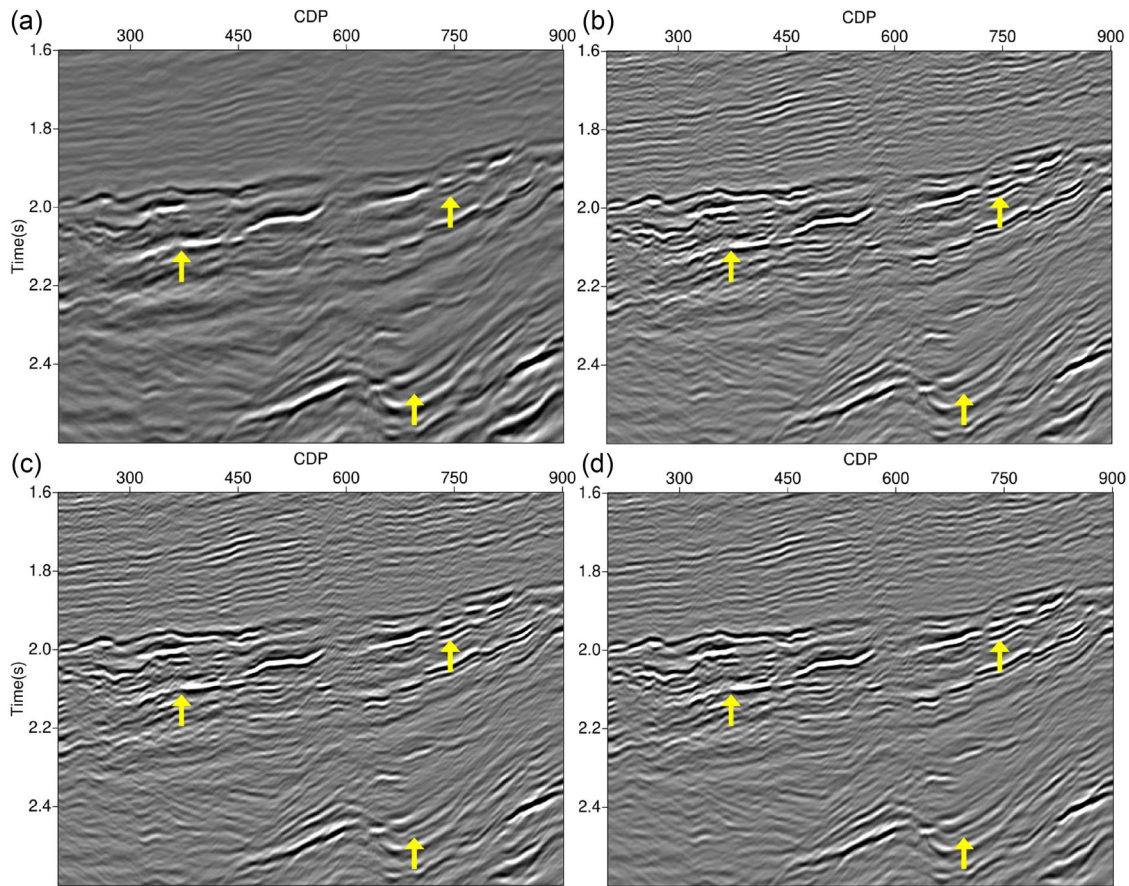


FIGURE 10 Comparison of the enlarged details in the lower box of Figure 8. Panel (a) shows the deep migration result obtained by conventional prestack time migration (PSTM). Panels (b)–(d) show the deep migration results obtained by Q model in deabsorption prestack time migration (QPSTM) in Figure 8b–d. Note the QPSTM results have higher resolution, providing a clearer description of the structure, as indicated by the arrow. Panels (b) and (c) resulted in a lower signal-to-noise compared to Panel (d) cause they did not consider the noise caused by Q compensation. The comparison of the amplitude spectrum is shown in Figure 11b. CDP, common depth point.

and improved performance on the validation set for Network-A and Network-B. These parameter choices enhance the models' training efficiency and performance, yielding more reliable deep learning models for future practical applications. Figures 5a and 6b present the training loss, validation loss and validation accuracy of Network-A, whereas Figure 5c,d presents the corresponding metrics for Network-B. The horizontal axis represents training iterations, which indicate the number of samples processed per iteration, and the vertical axis denotes loss or accuracy. The results show that as the number of training iterations increases, predictions gradually converge and losses decrease. After 50 iterations, Network-A's loss reduction convergence speed slows, and the accuracy on the validation set stabilizes, indicating that the network has reached convergence. Meanwhile, for Network-B, the loss reduction convergence speed slows after 150 iterations, whereas the validation set accuracy remains constant, indicating that the network has reached convergence. Unlike the conventional accuracy calculation method, the optimal Q_{eff} or $F3$ value is not definitive due to the subjectivity in assign-

ing training labels. Thus, we make the following assumption that

$$|\text{Index}_{\text{true}} - \text{Index}_{\text{predict}}| \leq 1. \quad (5)$$

When Equation (5) is satisfied, it represents a successful prediction. For example, if true Q_{eff} is ranked third and the predicted Q_{eff} is second, it is considered a successful prediction. The neural network training framework is implemented using PyTorch and trained on four GeForce RTX 2080 Ti GPUs, requiring approximately 3 h to complete training the entire network.

RESULT

We applied our scheme to a real 3D dataset from another region, which consists of 1131 (CDPs) \times 3000 (ms) with a common depth point (CDP) interval of 20 m and a temporal sampling interval of 4 ms, the offset ranges from 50 to

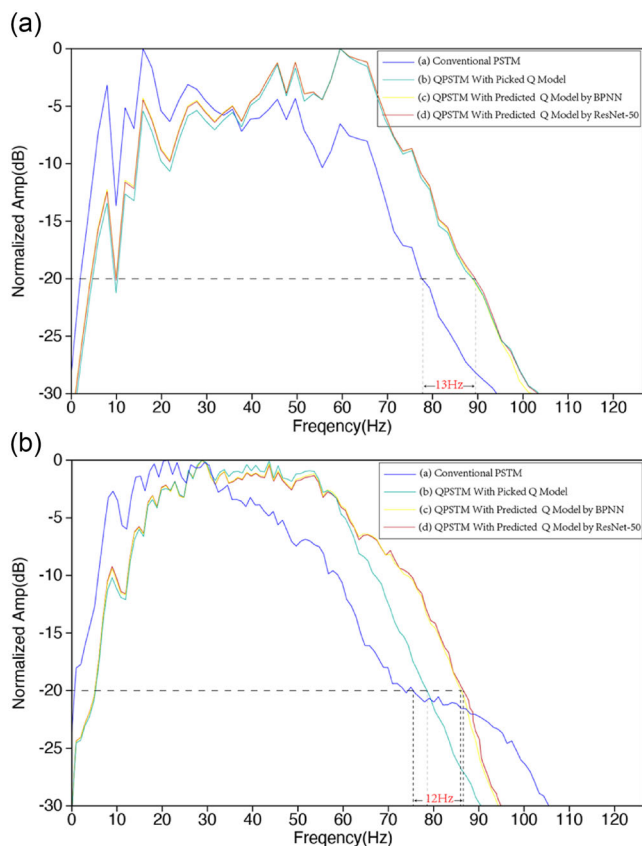


FIGURE 11 Comparison of the amplitude spectrum-related sections. Panel (a) is the comparison of the shallow section spectrum in Figure 9. Panel (b) compares the deep section spectrum in Figure 10. Note the frequency bandwidth of the Q model in deabsorption prestack time migration (QPSTM) result is increased by 13 Hz (upper parts) and 12 Hz (lower parts) at -20 dB compared to the conventional prestack time migration (PSTM) result, respectively. BPNN, back-propagation neural network.

4450 m with an interval of 100 m. The Q_{eff} sequence is obtained by taking the reciprocal of 15 Q values ranging from 0.0025 to 0.01 with equal intervals (Q_{eff} varies from 400 to 100). The Q_{eff} and $F3$ values are similar with training ($F3$ varies from 50 to 120 Hz with an interval of 5 Hz). Figure 6 shows the illustration of transfer learning. Figure 6a shows the training data. Transfer learning was performed on the existing network using another region data of Line 415 as shown in Figure 6b. Figure 6c shows the prediction data from the same region as transfer learning on Line 350. It was observed that the regional subsurface structure of the training data is very different from that of transfer learning and prediction. Subsequently, we selected multi-channel spectrum data and multi-channel section data from Line 350 for prediction.

Figure 7 compares the effective Q model of Line 350 obtained by manually picked, predicted by back-propagation neural network (BPNN) (Wu et al., 2024) and predicted by our approach. The Q fields are relatively consistent in most

regions. The prediction processing in Figure 7b,c uses denser grids than the manual processing in Figure 7a. However, our approach utilizes ResNet-50, which is deeper and more complex than BPNN, to better express the nonlinear mapping relationship between seismic sections and Q values. As a result, the Q fields between 1.5 and 2.5 s show more variation than Figure 7a,b, indicating subsurface detail information. The Q model shown in Figure 7a–c was applied to the Q model in deabsorption prestack time migration, and the migration stacked sections are shown in Figure 8b–d. Figure 8a shows the result obtained by conventional prestack time migration (PSTM), and comparing with Figure 8b–d, the deabsorption PSTM result gains higher resolution. Figures 9 and 10 further compare the migration results from the upper and lower boxes of Figure 8, respectively. We can see that the overlay events of deabsorption result are well separated and gain a clearer description of the structure as indicated by the arrow in Figure 9. However, compared to the migration result based on the method proposed in this paper, as shown in Figure 10d, the result from BPNN, as shown in Figure 10c, did not consider the noise caused by Q compensation, resulting in a lower signal-to-noise ratio. Figure 11 further compares the amplitude spectrum of related sections in Figures 9 and 10, and we can see that the frequency bandwidth increases by 13 Hz (upper parts) and 12 Hz (lower parts) at -20 dB, respectively.

CONCLUSION

We have presented a deep learning-based Q model building scheme that improves the effective Q estimation. The proposed scheme is developed by incorporating deep learning into the effective Q approach of deabsorption prestack time migration (QPSTM). Utilizing the robust nonlinear mapping capabilities of convolutional neural networks, we have established a nonlinear mapping relationship from migration sections and spectra to Q_{eff} and $F3$. The resulting scheme overcomes the difficulties of manual processing, including the concurrent determination of Q_{eff} and $F3$ and the substantial workload it entails. We consider the effective Q estimation as two multi-classification tasks with two networks. One of them determines the optimal $F3$ for a selected Q using multi-channel amplitude spectra, and the other is a residual neural network that determines the optimal Q using multi-channel imaging sections within the selected small window filtered by corresponding $F3$. As a result, we gained a Q model that improves the imaging resolution without amplifying noise.

We applied the scheme to a real dataset from another region with transfer learning on an existing network. Despite vast differences in subsurface geological structures across different regions, our network demonstrates considerable generalization capability via transfer learning. In comparison with conventional PSTM results, the QPSTM high-resolution

imaging results are obtained using the deep-learning-based Q model building scheme. High-quality and diverse training data are crucial for the model's generalizability across different geological environments. However, the transfer learning capabilities demonstrated by our method offer a promising path forward. This enables us to enhance the model's robustness by expanding the dataset to include various geological features and regions. Moreover, although our method has shown promising results in predicting Q values in the time domain, extending this approach to the depth domain remains an important work for further study in the future.

ACKNOWLEDGEMENTS

We thank the National Key R&D Program of China (grant no. 2020YFA0713402), the National Natural Science Fund of China (grant nos. 42174128 and 42030802) and Guangdong Provincial Key Laboratory of Geophysical High-resolution Imaging Technology (2022B1212010002) for supporting this work.

DATA AVAILABILITY STATEMENT

Research data are not shared.

ORCID

Xin Ju  <https://orcid.org/0009-0009-9346-2960>

REFERENCES

- Aki, K. & Richards, P.G. (1980) *Quantitative seismology: theory and methods*. San Francisco: W. H. Freeman.
- Dasgupta, R. & Clark, R.A. (1998) Estimation of Q from surface seismic reflection data. *Geophysics*, 63(6), 2120–2128. Available from: <https://doi.org/10.1190/1.1444505>
- De Boer, P.T., Kroese, D.P., Mannor, S. & Rubinstein, R.Y. (2005) A tutorial on the cross-entropy method. *Annals of Operations Research*, 134, 19–67.
- Gladwin, M.T. & Stacey, F.D. (1974) Anelastic degradation of acoustic pulses in rock. *Physics of the Earth and Planetary Interiors*, 8(4), 332–336. Available from: [https://doi.org/10.1016/0031-9201\(74\)90041-7](https://doi.org/10.1016/0031-9201(74)90041-7)
- He, F., Liu, T. & Tao, D. (2019) Control batch size and learning rate to generalize well: theoretical and empirical evidence. *Neural Information Processing Systems*. <https://dl.acm.org/doi/10.5555/3454287.3454390>
- He, K., Zhang, X., Ren, S. & Sun, J. (2016) Deep residual learning for image recognition. In: *Proceedings of the IEEE conference on computer vision and pattern recognition*, 27–30 June 2016, Las Vegas, NV, USA. New York City, IEEE. pp. 770–778. Available from: <https://doi.org/10.48550/arXiv.1512.03385>
- LeCun, Y., Bengio, Y. & Hinton, G. (2015) Deep learning. *Nature*, 521(7553), 436–444.
- Liu, W., Cheng, Q., Liu, L., Wang, Y. & Zhang, J. (2020) Accelerating high-resolution seismic imaging by using deep learning. *Applied Sciences*, 10(7), 2502. Available from: <https://doi.org/10.3390/app10072502>
- Li, F., Yu, Z. & Ma, J. (2024) An effective Q extraction method via deep learning. *Journal of Geophysics and Engineering*, 21, 483–495. Available from: <https://doi.org/10.1093/jge/gxae011>
- Li, J., Qu, Y., Li, Y., Huang, C. & Li, Z. (2024) Ocean bottom dual-sensor Q -compensated elastic least-squares reverse time migration based on acoustic and separated-viscoelastic coupling equations. *Geophysics*, 89(3), S155–S173. Available from: <https://doi.org/10.1190/geo2023-0433.1>
- Mittet, R., Sollie, R. & Hokstad, K. (1995) Prestack depth migration with compensation for absorption and dispersion. *Geophysics*, 60(5), 1485–1494. Available from: <https://doi.org/10.1190/1.1443882>
- O'Brien, P.N.S. & Lucas, A.L. (1971) Velocity dispersion of seismic waves. *Geophysical Prospecting*, 19(1), 1–26. Available from: <https://doi.org/10.1111/j.1365-2478.1971.tb00583.x>
- Park, M.J. & Sacchi, M.D. (2020) Automatic velocity analysis using convolutional neural network and transfer learning. *Geophysics*, 85(1), V33–V43. Available from: <https://doi.org/10.1190/geo2018-0870.1>
- Qu, Y., Wang, Y., Li, Z. & Liu, C. (2021) Q least-squares reverse time migration based on the first-order viscoacoustic quasidifferential equations. *Geophysics*, 86(4), S283–S298. Available from: <https://doi.org/10.1190/geo2020-0712.1>
- Qu, Y., Zhu, J., Chen, Z., Huang, C., Wang, Y. & Liu, C. (2022) Q -compensated least-squares reverse time migration with velocity-anisotropy correction based on the first-order velocity-pressure equations. *Geophysics*, 87(6), S335–S350. Available from: <https://doi.org/10.1190/geo2021-0689.1>
- Sun, J., Fomel, S., Zhu, T. & Hu, J. (2016) Q -compensated least-squares reverse time migration using low-rank one-step wave extrapolation. *Geophysics*, 81(4), S271–S279. Available from: <https://doi.org/10.1190/geo2015-0520.1>
- Wang, J., Liu, W., Zhang, J. & Zhao, Z. (2017) Building a heterogeneous Q model: an approach using surface reflection data. *Journal of Seismic Exploration*, 26(4), 293–310.
- Wang, J., Xiao, Z., Liu, C., Zhao, D. & Yao, Z. (2019) Deep learning for picking seismic arrival times. *Journal of Geophysical Research: Solid Earth*, 124(7), 6612–6624. Available from: <https://doi.org/10.1029/2019JB017536>
- Wang, J., Lu, W. & Li, Y. (2021) A multitask learning-based dynamic wavelet amplitude spectra extraction method and its application in Q estimation. *IEEE Transactions on Geoscience and Remote Sensing*, 60, 1–10. Available from: <https://doi.org/10.1109/TGRS.2021.3086266>
- Wu, J., Shi, Y., Wang, W., Li, S. & Yang, Q. (2024) Improving image resolution using deabsorption prestack time migration with effective Q estimation: a back-propagation network approach. *Geophysics*, 89(1), S71–S82. Available from: <https://doi.org/10.1190/geo2022-0753.1>
- Xin, K. & Hung, B. (2009). 3-D tomographic Q inversion for compensating frequency dependent attenuation and dispersion. SEG Technical Program Expanded Abstracts. 28. 4014–4018. [10.1190/1.3255707](https://doi.org/10.1190/1.3255707)
- Xu, J., Liu, W., Wang, J., Liu, L. & Zhang, J. (2018) An efficient implementation of 3D high-resolution imaging for large-scale seismic data with GPU/CPU heterogeneous parallel computing. *Computers & Geosciences*, 111, 272–282. Available from: <https://doi.org/10.1016/j.cageo.2017.11.020>
- Yildırım, E., Saatçılar, R. & Ergintav, S. (2017) Estimation of seismic quality factor: artificial neural networks and current approaches. *Journal of Applied Geophysics*, 136, 269–278. Available from: <https://doi.org/10.1016/j.jappgeo.2016.11.010>

- Zhang, H., Han, J., Li, Z. & Zhang, H. (2021) Extracting Q anomalies from marine reflection seismic data using deep learning. *IEEE Geoscience and Remote Sensing Letters*, 19, 1–5. Available from: <https://doi.org/10.1109/LGRS.2020.3048171>
- Zhang, J., Li, Z., Liu, L., Wang, J. & Xu, J. (2016) High-resolution imaging: an approach by incorporating stationary-phase implementation into deabsorption prestack time migration-n. *Geophysics*, 81(5), S317–S331. Available from: <https://doi.org/10.1190/geo2015-0543.1>
- Zhang, J., Wu, J. & Li, X. (2013) Compensation for absorption and dispersion in prestack migration: an effective Q approach. *Geophysics*, 78(1), S1–S14. Available from: <https://doi.org/10.1190/geo2012-0128.1>
- Zhang, J. & Wapenaar, K. (2002) Wavefield extrapolation and prestack depth migration in anelastic inhomogeneous media. *Geophysical Prospecting*, 50(6), 629–643. Available from: <https://doi.org/10.1046/j.1365-2478.2002.00342.x>
- Zhang, J., Li, J. & Cheng, W. (2022) Simultaneous interval- Q estimation and attenuation compensation based on fusion deep neural network. *IEEE Transactions on Geoscience and Remote Sensing*, 60, 1–9. Available from: <https://doi.org/10.1109/TGRS.2022.3211299>
- Zhou, C., Wang, S., Wang, Z. & Cheng, W. (2022) Absorption attenuation compensation using an end-to-end deep neural network. *IEEE Transactions on Geoscience and Remote Sensing*, 60, 1–9. Available from: <https://doi.org/10.1109/TGRS.2022.3190407>
- Zhu, T., Harris, J.M. & Biondi, B. (2014) Q -compensated reverse-time migration. *Geophysics*, 79(3), S77–S87. Available from: <https://doi.org/10.1190/geo2013-0344.1>

How to cite this article: Ju, X., Xu, J. & Zhang, J. (2024) Deep-learning-based Q model building for high-resolution imaging. *Geophysical Prospecting*, 1–13. <https://doi.org/10.1111/1365-2478.13616>